## Open Archive Toulouse Archive Ouverte

OATAO is an open access repository that collects the work of Toulouse researchers and makes it freely available over the web where possible

This is an author's version published in: http://oatao.univ-toulouse.fr/20860

# On the stability of the oxides film formed on a magnesium alloy containing rare-earth elements

Samuel Leleu [a, b], Bertrand Rives [b], Jérôme Bour [c], Nicolas Causse [a], Nadine Pébère [a, *]

[a] CIRIMAT, Université de Toulouse, CNRS, INPT, UPS, ENSIACET, 4 allée Emile Monso, BP44362, 31030, Toulouse cedex 4, France
[b] IRT Saint Exupéry, 118 route de Narbonne - CS 44248, 31432, Toulouse, France
[c] LIST, 41, rue du Brill, 4422, Belvaux, Luxembourg

## ABSTRACT

The electrochemical behaviour of a commercial magnesium alloy containing rare-earth elements, the WE43, was investigated by electrochemical techniques in both sulphate and chloride solutions and compared to that of pure magnesium (99.95 wt %). A particular attention was paid to the oxides film that formed during the corrosion process. Electrochemical impedance data analysis allowed the oxides films thickness to be determined. The film was thinner and more protective for the WE43 Mg alloy than for the pure Mg. ToF-SIMS analysis showed the incorporation of alloying elements, mainly yttrium and zirconium in the corrosion products layer. A higher compactness due to a higher Pilling-Bedworth ratio can explain the electrochemical results.

## 1. Introduction

Magnesium alloys are known to have a high strength-to-weight ratio amongst other structural materials [1,2]. However, their use is still limited in the transport industries (automotive and aircraft) due to their poor corrosion resistance and low ignition point [3]. For the WE43 alloy (Mg-Y-Nd-Zr), addition of rare-earth (RE) elements, especially Y, and an appropriate heat treatment improved its fire resistance and its mechanical properties (*i.e.* tensile strength and creep) at ambient and high temperature (up to 300 °C) [4–6].

Most of alloying elements have limited solubility in Mg and therefore all commercial Mg alloys contain intermetallics which act as local cathodes and consequently increase their corrosion rate. However, the better corrosion resistance of Mg-Al alloys has been partly explained in terms of increased passivity by incorporation of aluminium oxide which stabilizes the magnesium oxide layer, even though the layer is thinner when the amount of Al is increased [7]. Nordlien et al. have concluded, from transmission electron microscopy observations, that alloying Mg-Al alloys with rare-earth elements improved the passive properties of the oxide film by reducing the degree of hydration and by increasing the resistance against cation transport [8]. However, this effect was mainly attributed to the presence of aluminium as a major alloying element. For an AZ91 Mg alloy, it was shown that the progressive dissolution of the $\alpha$-eutectic phase led to a strong aluminium enrichment of the corrosion product layer and, when a threshold has been reached in the level of $Al_2O_3$ in the magnesium oxide (or hydroxide) layer, a change of phenomenology has been observed in the impedance diagrams [9]. Studying the atmospheric corrosion of Mg alloys at different temperatures, Esmaily et al. [10] observed an Al enrichment of the corrosion film, associated to oxidized aluminium ($Al^{3+}$) and a depletion of Al immediately below the film.

It has been shown that intermetallics containing RE elements (Y, Nd or Zr) were always cathodic by comparison with the Mg matrix [11–17], except in a recent study of Liu et al. [18]. On the other hand, it was generally reported that the presence of RE elements in solid solution in Mg alloys conferred better protection due to the formation of more protective films [19–23]. Some authors claimed that small addition of Y (less than 0.8 wt %) improved the corrosion resistance of an AZ91 alloy while higher content (2 wt %) was detrimental [14,24,25]. Liu et al. studied the corrosion of several binary Mg-Y alloys in NaCl or $Na_2SO_4$ solutions [26]. In the $Na_2SO_4$ solution, the authors found that the corrosion resistance increased with increasing Y content (in the range 3–7% Y), linked to the stability of the surface film in a mild environment. In contrast, in

the NaCl solution, the authors showed that the corrosion rate increased with increasing Y content, attributed to higher amounts of Y-containing intermetallic particles [26]. Takenaka et al. showed that the corrosion resistance of Mg was greatly improved by adding small amounts of RE (La, Nd, Ce), whereas for an RE excess, the corrosion resistance was deteriorated [21]. Zucchi et al. compared the electrochemical behaviour of a WE43 Mg alloy with that of pure Mg in diluted chloride or sulphate media [27]. They also concluded that the presence of RE elements improved the tendency of Mg to passivation. From the film capacitance, roughly estimated from the impedance diagrams, the authors showed that a thinner and more protective film was formed on the WE43 alloy by comparison with pure Mg [27]. Pinto et al. studied the behaviour of a WE54 alloy and two other Mg-RE alloys (ZK31 and EZ33) in alkaline media (pH = 13) with or without $Cl^-$ ions [22]. The highest charge transfer resistance was found for the WE54 alloy and attributed to the formation of a more protective film. For the three Mg alloys, the authors have observed that the impedance diagrams were not affected by the presence of chlorides [22]. Ardelean et al. used X-ray photoelectron spectroscopy (XPS) and time-of-flight secondary ion mass spectrometry (ToF-SIMS) to study the composition of the corrosion products layer formed on a WE43 alloy surface [28]. They showed that the inner MgO film was enriched with $Y_2O_3$ and $Y(OH)_3$ and in small amount of $MgH_2$, $ZrO_2$ and $Nd_2O_3$. The authors found that, in a $Na_2SO_4$ solution, the corrosion rate was lower for the WE43 alloy compared to an AZ91 alloy or to pure Mg. It was recently shown that the addition of Li (wt % > 11) induced a limitation of the anodic dissolution which was mainly attributed to the formation of a carbonate-rich surface film [29].

Finally, the literature emphasized that the corrosion resistance of rare-earth Mg alloys is controlled by two antagonist effects: higher cathodic activity of the intermetallic particles containing rare-earths and formation of more protective surface films. Depending of the rare-earth content, the protection by the oxides/hydroxides films would not be sufficient to counterbalance the detrimental effect of the galvanic coupling between the particles and the matrix. The electrolyte, particularly the presence of chlorides also played an important role. These combination effects are not yet fully understood.

The aim of the present work was to investigate the behaviour of a commercial WE43 Mg alloy and more particularly to better understand the role played by the corrosion products layer on its corrosion resistance. Current-voltage curves and electrochemical impedance measurements were performed with a rotating disk electrode (RDE) in aerated $Na_2SO_4$ or NaCl solutions. Pure Mg was also used for comparison. From impedance data analysis, the oxides films thickness was determined [30–33]. The composition of the corrosion products formed on the WE43 alloy surface was analysed by time-of-flight secondary ion mass spectrometry (ToF-SIMS).

## 2. Experimental

### 2.1. Materials

Pure Mg was purchased from Alfa Aesar with a purity of 99.95% (250 ppm Fe; 20 ppm Al; 20 ppm Cu; 46 ppm Mn). The WE43 Mg alloy was provided by Prodem-Bonnans Company in the T6 thermal condition. Its composition is given in Table 1 in accordance with the ASTM B951-11. For the electrochemical measurements, the working electrodes (pure Mg or WE43 alloy) were rotating disks of 1 $cm^2$ surface area consisting of the cross-section of cylindrical rods. The lateral part of the rods were covered with a heat-shrinkable sheath leaving only the tip in contact with the solution. The samples were abraded with successive SiC papers (grade 4000), cleaned in ethanol in an ultrasonic bath and finally dried in warm air.

**Table 1**

Chemical composition (wt %) of the WE43 Mg alloy in accordance with ASTM B951-11, other rare earths (ORE) shall principally be La, Ce, Pr, Nd, Gd, Dy, Er, Yb.

| Y | Nd | Zr | Zn | ORE | Mg |
|---|---|---|---|---|---|
| 3.7–4.3 | 2.0–2.5 | 0.4–1 | 0.2 | 1.9 | Bal. |

The corrosive media were prepared from deionised water by adding 0.1 M $Na_2SO_4$ or 0.2 M NaCl (analytical grade VWR Chemicals reagents, AnalaR NORMAPUR).

### 2.2. Microstructure characterization

A LEO 435VP scanning electron microscope (SEM) was used for microstructure characterization of the WE43 Mg alloy. Semi-quantitative analysis was performed by energy dispersive X-ray spectroscopy (EDX) with a Ge detector (Imix-PC, PGT). EDX analyses were performed over different locations on the WE43 alloy surface to determine the mean chemical composition of the regions of interest. Prior to the observations, the sample surface was abraded with successive SiC papers (grade 4000), diamond pastes and $SiO_2$ colloidal suspension (Struers OP-S 0.04 μm). Then, it was etched with an acetic-glycol solution composed of: 20 mL acetic acid +1 mL nitric acid +60 mL ethylene glycol +20 mL distilled water. The acids were purchased from VWR Chemicals and the ethylene glycol from PanReac Applichem.

### 2.3. Electrochemical measurements

A classical three-electrode cell was used with a platinum grid auxiliary electrode, a saturated sulphate reference electrode (MSE) or saturated calomel electrode (SCE) and the rod of the WE43 alloy or the pure Mg sample as rotating disk electrode (RDE). The rotation rate was kept at 250 rpm. Current-voltage curves were obtained using a Solartron 1287 electrochemical interface. They were plotted consecutively from the cathodic to the anodic range (from −0.5 V *vs.* the corrosion potential ($E_{corr}$) to + 0.5 V/MSE). The potential sweep rate was fixed at 10 mV $min^{-1}$. The polarisation curves were corrected from the ohmic drop, based on the electrolyte resistance determined from the impedance diagrams. Electrochemical impedance measurements were carried out using a Solartron 1287 electrochemical interface connected to a Solartron 1250 frequency response analyser (FRA). Impedance diagrams were obtained under potentiostatic regulation, at the corrosion potential ($E_{corr}$), over a frequency range of 65 kHz to a few mHz with 8 points per decade, using a 30 $mV_{rms}$ sinusoidal voltage. The linearity was checked by varying the amplitude signal. At least two experiments were performed. The obtained impedance diagrams were always consistent with the Kramers-Kronig relations [34].

### 2.4. ToF-SIMS analysis

The analyses were performed using a TOF SIMS V (IonTOF, Münster, Germany) operating at a pressure of $10^{-9}$ mbar. Mass spectra and imaging experiments were carried out with a 25 keV pulsed $Bi_3^+$ cluster ion source, delivering 0.40 pA target current. For the sputtering in dynamic SIMS applications (depth profiling, 3D imaging), a 10 keV $Cs^+$ source was used with 31 nA target current. For depth profiles, the sputtered crater size was 500 μm × 500 μm and only a 300 μm × 300 μm area was analysed in the middle of the sputtered area. To compensate the charging effect during the depth profile measurement, a low energy electron flood gun was used. The data were obtained in negative mode and the secondary ion mass spectra were calibrated using $Cn^-$ carbon clusters.

## 3. Results

### 3.1. Microstructure of the WE43 Mg alloy

A SEM micrograph of the WE43 Mg alloy is presented in Fig. 1. It reveals the α-Mg matrix with large grains (10–100 μm). Inside most of the grains, whitish "clouds" are noticeable in back-scattered electron (BSE) mode (arrow 1). Semi-quantitative EDX analysis was performed over two zones: the Mg matrix and the whitish "clouds". The results are reported in Table 2. The matrix was found to be mainly enriched in Y, with small additions of Nd and Zr. The "whitish" clouds are enriched in Zr and slightly depleted in Mg, Y and Nd by comparison with the matrix. The significant concentration of Zr in the whitish zones was previously attributed to a redistribution of this element due to the thermal treatment [35]. Small precipitates appearing in bright on the micrograph are heterogeneously distributed both in the grain and at the grain boundaries (GBs). According to the literature, different morphologies can be observed: rectangular or irregular shape particles. The rectangular particles are Y-rich, likely $Mg_{24}Y_5$ intermetallic phase [11,36,37] and the irregular particles contain Zr [34–38]. An additional acicular sub-micronic secondary phase, barely visible by SEM, have been identified as β-$Mg_{14}Nd_2Y$ [37,38] or $Mg_{41}(Nd,Y)_5$ and $Mg_{24}(Y,Nd)_5$ [39].
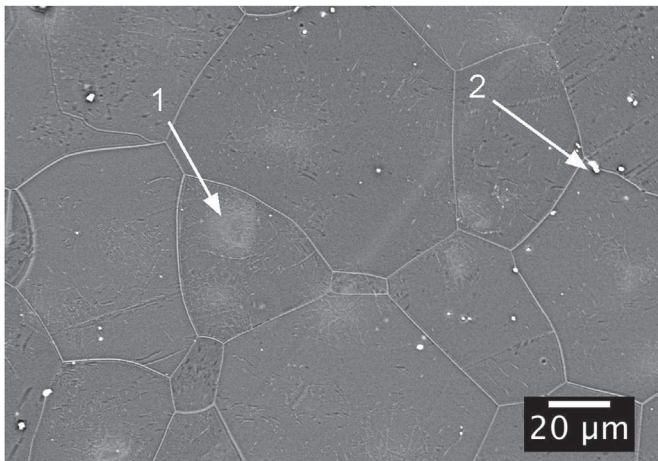


**Fig. 1.** SEM micrograph (back-scattered electron (BSE) mode) of the WE43 Mg alloy after polishing and chemical etching. (1) Zr-rich zone and (2) small Zr or Y precipitates. EDX data are provided in Table 2.

**Table 2**
Chemical compositions (wt %) of the Mg matrix and of the Zr-rich zone for the WE43 Mg alloy obtained by semi-quantitative EDX analysis.

|            | Mg   | Y   | Nd  | Zr  |
|------------|------|-----|-----|-----|
| α-matrix   | 93.1 | 4.6 | 1.9 | 0.3 |
| Zr-rich zone (1) | 90.6 | 3.9 | 1.6 | 3.9 |

### 3.2. Current-voltage curves

The polarisation curves for the WE43 alloy and for three immersion times at $E_{corr}$ in 0.1 M $Na_2SO_4$ are presented in Fig. 2. In the cathodic range (water reduction reaction), the three curves are superimposed showing that the cathodic reaction is unaffected by the immersion time. In contrast, in the anodic range, the current densities significantly decrease between 1 h and 24 h of immersion. Thus, when the immersion time increases, $E_{corr}$ is shifted towards
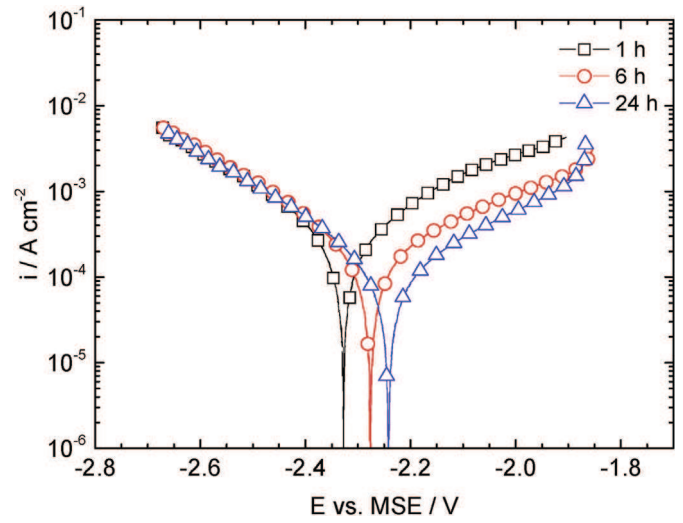


**Fig. 2.** Polarisation curves obtained for the WE43 Mg alloy after 1, 6, and 24 h at $E_{corr}$ in a 0.1 M $Na_2SO_4$ solution.



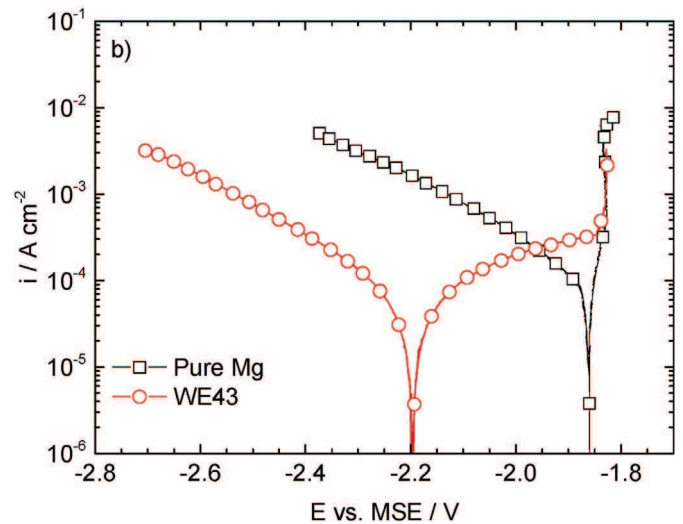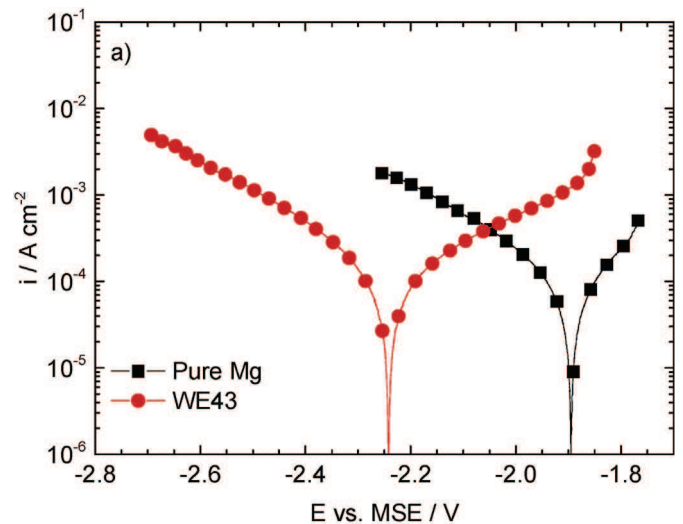**Fig. 3.** Polarisation curves obtained for the pure Mg and for the WE43 Mg alloy after 24 h of immersion at $E_{corr}$ in: (a) 0.1 M $Na_2SO_4$ and (b) 0.2 M NaCl.

more anodic values. These results can be attributed to the progressive formation of a partially protective film on the alloy surface, which decreases the active surface area and as a consequence the corrosion rate decreases [40–47]. The film is assumed to be composed mainly of $MgO/MgOH_2$ [40–47] and should be enriched in Y, Nd and Zr, which are the main elements in the magnesium matrix (Table 2). In the anodic range, linear parts can be observed. After 24 h of immersion, and around +400 mV vs $E_{corr}$, an inflexion point is seen, generally attributed to the breakdown of the oxides film formed on the alloy surface [47–50].

To study the influence of the electrolytic solution on the corrosion behaviour of the WE43 alloy, the polarisation curves were obtained in a $Na_2SO_4$ solution or in a NaCl solution after 24 h of immersion at $E_{corr}$ and compared to those obtained for the pure Mg (Fig. 3). In the NaCl solution (Fig. 3b), for an easier comparison, the potentials were given relative to the MSE. In the two media, it can be seen that $E_{corr}$ for the WE43 alloy is significantly shifted in the cathodic direction by comparison with the pure Mg. This shift (about 350 mV) was already reported in the literature and attributed to the presence of Zr in the Mg matrix [16]. Independently of the electrolyte and for both metals, the cathodic branch is rather similar. For the WE43 alloy, both in the $Na_2SO_4$ and in the NaCl solutions, the anodic curves show linear parts on a large potential domain. In the NaCl solution (Fig. 3b), and for a potential value of −1.85 V/MSE, an abrupt increase of the current densities is observed for both metals. For the pure Mg (Fig. 3b), this significant increase of current occurs close to $E_{corr}$ and at +50 mV vs. $E_{corr}$, the current density is about 10 mA cm$^{-2}$. This can be attributed to the breakdown of the oxides film indicating that its stability is affected by the presence of Cl$^-$. In the $Na_2SO_4$ solution, a breakdown potential can be also observed for both the alloy and the pure Mg but the currents increase was slower (Fig. 3a). It is generally accepted that Cl$^-$ are more aggressive than $SO_4^{2-}$ anions. This was partly explained by a higher ability of Cl$^-$ (designed as chaotrope) than $SO_4^{2-}$ (designed as cosmotrope) to dehydrate [51,52].

### 3.3. Electrochemical impedance measurements

The impedance diagrams (Nyquist coordinates) obtained for the pure Mg and for the WE43 alloy after 24 h in 0.1 M $Na_2SO_4$ and in 0.2 M NaCl are shown in Fig. 4. The diagrams are characterized by the presence of three time constants. The high-frequency capacitive loop results from both charge transfer and a film effect; the second one, at mid frequency, corresponds to the diffusion of Mg$^{2+}$ species through the porous hydroxide layer [42–44]. The inductive loop at low frequency would be ascribed to the existence of relaxation process of adsorbed species [42–44,53]. The impedance values are higher in the case of the WE43 alloy and independent of the electrolytic solution. In the case of pure Mg and in the presence of chloride ions (Fig. 4a), the impedance is lower compared to that of the WE43 alloy and the mid frequency loop is barely visible. These results are in agreement with the anodic behaviour of the two materials observed on the polarisation curves (Fig. 3).

The values of the charge transfer resistance ($R_T$) associated to the first capacitive loop were graphically determined for the pure Mg and the WE43 alloy in the chloride and in the sulphate media. They are reported as a function of the immersion time in Fig. 5. For the pure Mg, the $R_T$ value stabilizes after 24 h of immersion at about 275 $\Omega$ cm$^2$ in the $Na_2SO_4$ solution and 70 $\Omega$ cm$^2$ in the NaCl solution. For the WE43 alloy, the $R_T$ values are identical in the two media: during the first 24 h of immersion, $R_T$ increases to reach a value of around 400 $\Omega$ cm$^2$ and then, beyond 24 h, $R_T$ continues to increase to reach values of 600 $\Omega$ cm$^2$, 800 $\Omega$ cm$^2$ and 900 $\Omega$ cm$^2$ after 72 h, 240 h and 360 h of immersion, respectively (not shown to keep identical scales in Fig. 5a and 5b). The higher $R_T$ values in the case of
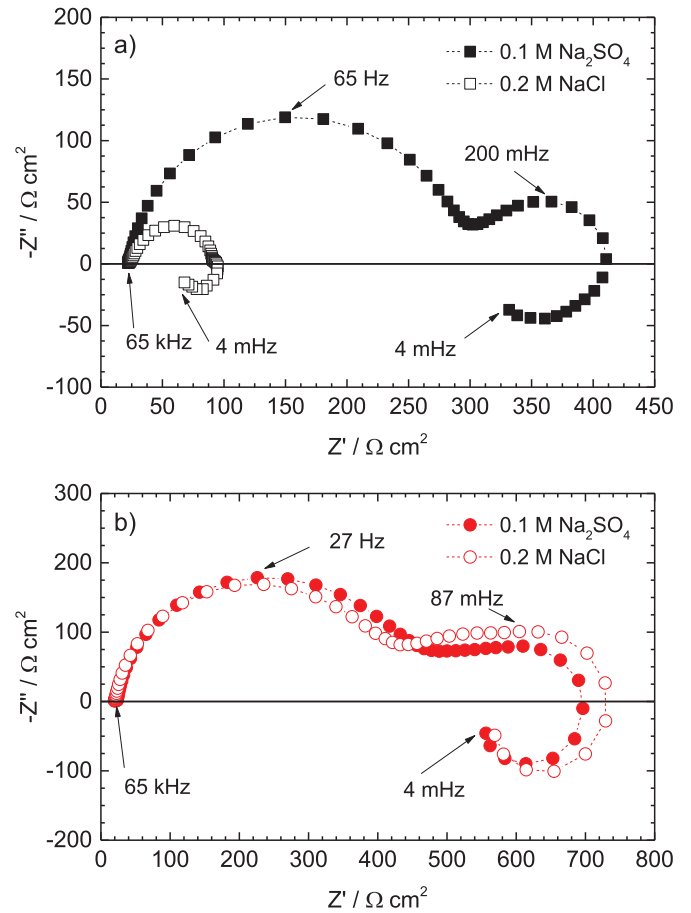


**Fig. 4.** Electrochemical impedance diagrams obtained after 24 h of immersion at $E_{corr}$ in 0.1 M $Na_2SO_4$ or 0.2 M NaCl for: (a) the pure Mg and (b) the WE43 Mg alloy.

the WE43 alloy might indicate a higher coverage by the oxides/hydroxides layer by comparison with the pure Mg.
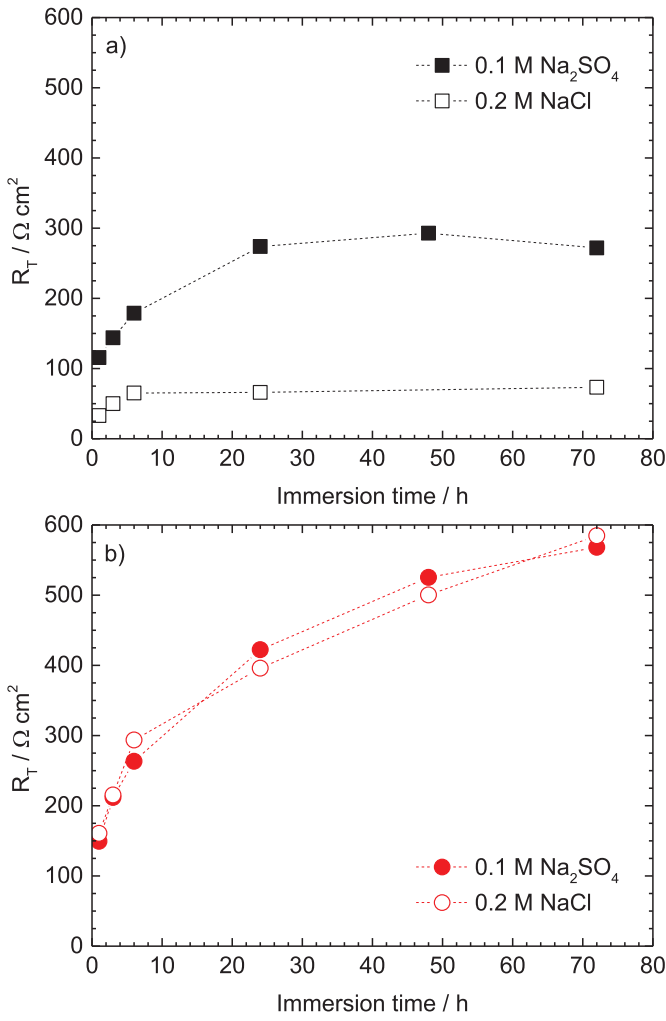
Instantaneous corrosion current densities ($i_{corr}$) after 24 h of immersion were calculated by using the Stern-Geary relationship [54]:

$$i_{corr} = \frac{b_a b_c}{2.303(b_a + b_c)R_T} = \frac{B}{R_T} \qquad (1)$$

where $b_a$ and $b_c$ are the anodic and cathodic Tafel slopes, respectively. $B = (1/2.303) (b_a \ b_c)/(b_a + b_c)$. $R_T$ is the charge transfer resistance. The $R_T$, B and $i_{corr}$ values are reported in Table 3. It can be seen that in the $Na_2SO_4$ solution, $i_{corr}$ is in the same order of magnitude for the alloy and for the pure Mg. In contrast, in the NaCl solution, $i_{corr}$ is about three times higher for the pure Mg than for the WE43 alloy. The electrode surfaces were observed after 72 h of immersion in the NaCl solution for both materials (Fig. 6). The photographs show that the pure Mg electrode surface is strongly attacked and rough whereas the WE43 alloy surface appears dull and relatively smooth. For the WE43 Mg alloy, the corrosion seems to be developed more homogeneously.

Electrochemical measurements and visual observations of the samples clearly indicated that the pure Mg is strongly susceptible to chloride ions and conversely, for the WE43 alloy, electrochemical results did not show any major differences between the two media. Similar results have been already reported [20,46].

Then, the high-frequency part of the impedance diagrams was analysed to obtain additional information on the formation and on

**Fig. 5.** Charge transfer resistance ($R_T$) versus immersion time in a 0.1 M Na$_2$SO$_4$ or NaCl 0.2 M for: (a) the pure Mg and (b) the WE43 Mg alloy.

**Fig. 6.** Visual observations of the electrode surfaces after 72 h of immersion in 0.2 M NaCl for: (a) the pure Mg and (b) the WE43 Mg alloy.

**Table 3**
Instantaneous corrosion current densities calculated from the Stern-Geary relationship (Eq. (1)) for the pure Mg and for the WE43 Mg alloy after 24 h of immersion in a Na$_2$SO$_4$ or NaCl solution.

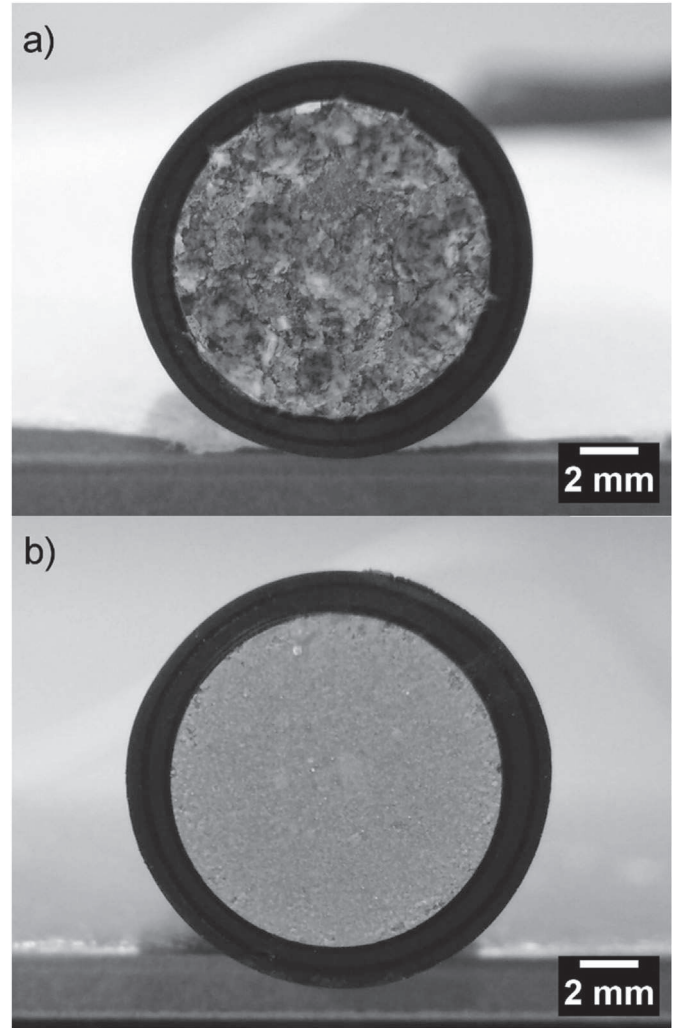|  | $R_T$ ($\Omega$ cm$^2$) | $B$ (mV) | $i_{corr}$ ($\mu$A cm$^{-2}$) |
|---|---|---|---|
| Mg/Na$_2$SO$_4$ | 273 ± 5 | 36 ± 2 | 132 ± 8 |
| Mg/NaCl | 67 ± 5 | 36 ± 2 | 537 ± 28 |
| WE43/Na$_2$SO$_4$ | 418 ± 5 | 64 ± 2 | 153 ± 5 |
| WE43/NaCl | 406 ± 5 | 64 ± 2 | 158 ± 5 |

the properties of the films. In the case of oxide films, the capacitance of the layer ($C_{ox}$) can be extracted from the impedance data by using the complex-capacitance representation, without using any model [30−33,55]:

$$C(\omega) = \frac{1}{j\omega[Z(\omega) - R_e]} \qquad (2)$$

with $\omega = 2\pi f$ and $R_e$, is the electrolyte resistance.

First, the $R_e$ value must be accurately determined from the extrapolation at high-frequency on the real axis of the Nyquist diagram to correctly represent the complex-capacitance. As an example, Fig. 7 presents the complex-capacitance plots for the pure

Mg and for the WE43 alloy after 48 h of immersion in the Na$_2$SO$_4$ solution. Capacitances were determined by extrapolation of the high-frequency data to the real axis (vertical line crossing the C′ axis (C″ = 0) as shown in Fig. 7). This methodology leads to an overestimation of the $C_{ox}$ values [55]. In Fig. 7, it can be seen that the value obtained for the WE43 alloy (around 5 $\mu$F cm$^{-2}$) is higher than that obtained for the pure Mg (around 4 $\mu$F cm$^{-2}$). The $C_{ox}$ values were determined for different immersion times. For the pure Mg in the NaCl solution, it was not possible to extract the capacitance values due to dispersion of the points in the high-frequency range. Fig. 8a compares the time-dependence of the capacitances. First, it can be seen that $C_{ox}$ always decreases during the first 24 h of immersion and then stabilizes. From 24 h of immersion, $C_{ox}$ remains stable that might indicate that a large part of the electrode surface was covered by the oxides film. In agreement with the variation of the charge transfer resistance with time (Fig. 5), it can be assumed that the oxides film laterally grows on the electrode surface. It must be underlined that before 24 h of immersion, the double-layer capacitance might not be negligible in comparison with the oxides film capacitance [44]. Assuming that the oxides film is mainly composed of MgO, its thickness, $\delta_{ox}$, can be calculated from the relationship:
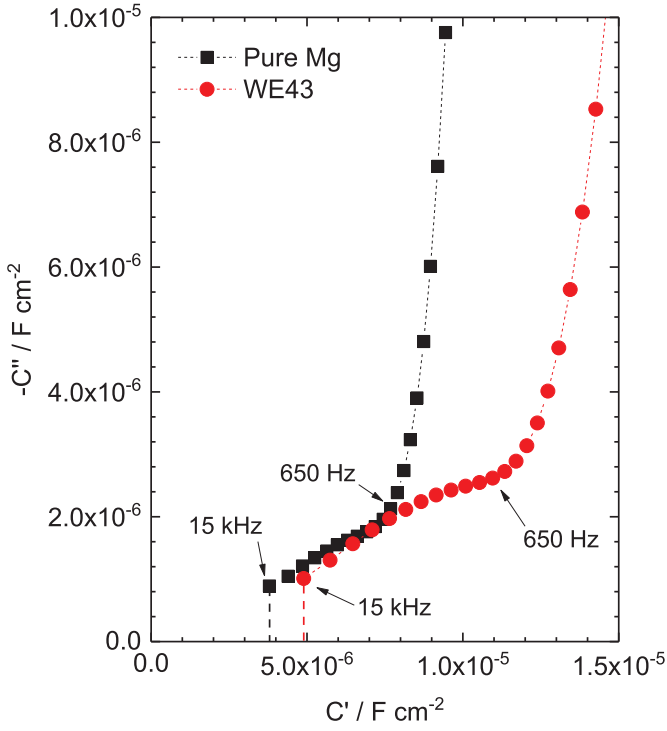
**Fig. 7.** Complex-capacitance plots corresponding to the impedance spectra of the pure Mg and the WE43 Mg alloy obtained after 48 h of immersion at $E_{corr}$ in 0.1 M $Na_2SO_4$ solution.

$$\delta_{ox} = \frac{\varepsilon \varepsilon_0}{C_{ox}} \tag{3}$$

where $\varepsilon$ is the dielectric permittivity of the MgO ($\varepsilon = 10$ [56]) and $\varepsilon_0$ is the vacuum permittivity. From the estimation of $C_{ox}$, $\delta_{ox}$ varied from 2.1 to 2.5 nm for the pure Mg, in agreement with the range of 3−5 nm, estimated by TEM [47], from 1.6 to 1.9 nm for the WE43 alloy in the $Na_2SO_4$ solution and from 1.2 to 1.5 nm in the NaCl solution (Fig. 8b).

### 3.4. ToF-SIMS analysis

The ToF-SIMS depth profiles obtained on the WE43 Mg alloy after 144 h of immersion in 0.1 M $Na_2SO_4$ are shown in Fig. 9. The first 100 s of sputtering corresponds to the stabilization of the dynamic regime and are not taken into account. $MgO^-$, $MgOH^-$ and $MgO_2H^-$ fragment ions have the most intense signals, associated with the existence of the $MgO/Mg(OH)_2$ layer. The $MgOH^-$ and $MgO_2H^-$ fragment ions are characteristic of brucite. The $MgO^-$ signal remains stable until 7500 s and increases until the end of the experiment, whereas the $MgO_2H^-$ and the $MgOH^-$ signals slowly decrease from about 400 s of sputtering. The presence of $SO_2^-$ and $SO_3^-$ signals throughout the depth profiles indicates the presence of the electrolyte salt in the corrosion products layer. Their intensities progressively decrease through the layer as approaching the metal/film interface. $YO^-$ and $ZrO^-$ signals continuously increase with the sputtering time, particularly during the first 2000 s. A weak signal attributed to the $NdO^-$ fragment ion is also detected. This indicates an enrichment in Zr and Y of the inner part of the film and a smaller enrichment in Nd of the outer part. The 3D chemical imaging of selected fragment ions: $MgO^-$, $MgO_2H^-$, $YO^-$ and $ZrO^-$ are presented in Fig. 10 for four sputtering times. The 3D representation
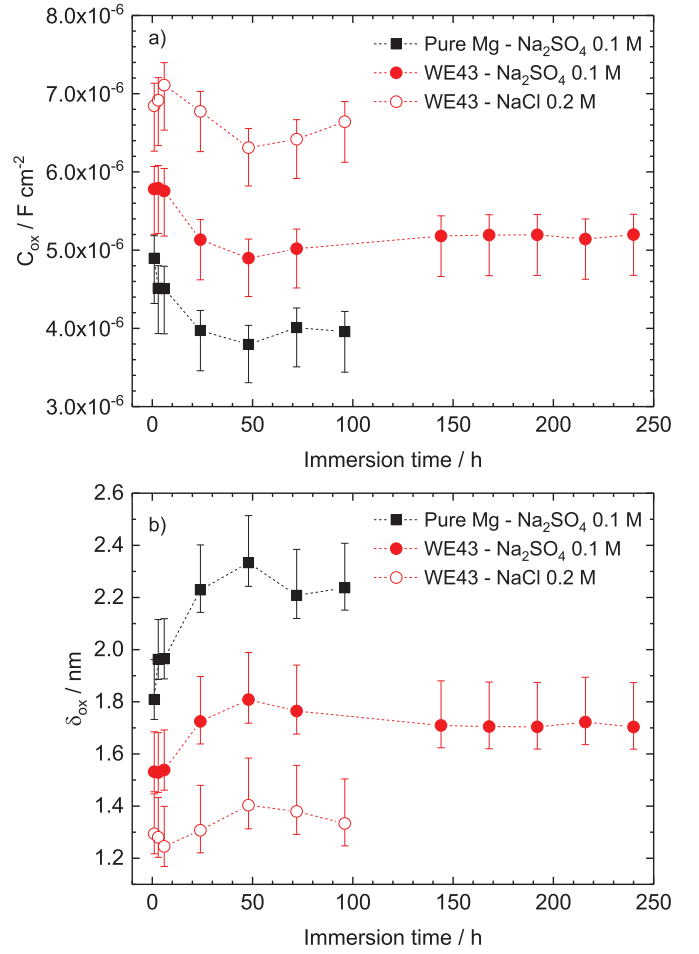


**Fig. 8.** (a) Oxides film capacitance ($C_{ox}$) obtained from the complex-capacitance plots and (b) oxides film thickness ($\delta_{ox}$) calculated according to Eq. (3) as function of immersion time for the pure Mg and the WE43 Mg alloy in 0.1 M $Na_2SO_4$ and for the WE43 Mg alloy in 0.2 M NaCl. Errors bars account for the uncertainty on the determination of the capacitance values at high-frequency.

allows the layer composition to be better visualised. First, it must be mentioned that after 144 h of immersion in the electrolyte, the WE43 alloy surface appeared cracked and the cracks seemed to correspond to the grain boundaries (GBs) (Fig. 1). All the 3D images confirmed the presence of these cracks (dark zones in the $YO^-/ZrO^-$ chemical imaging). This would indicate a difference of reactivity between the Mg matrix and the GBs. The $MgO^-$ signal is only observed above the Mg matrix whereas the $MgO_2H^-$ fragment ion is more visible in the cracked areas, particularly close to the metal/film interface. This might indicate that the Mg matrix is partially protected by the oxides layer and the dissolution would proceed at the GBs. Local inhomogeneity in the GBs and the presence of noble intermetallic particles (Fig. 1) could serve as local cathodes, favouring the formation of hydroxyl ions and the precipitation of $MgOH_2$ in these areas [36]. $ZrO^-$ is only localized in some regions of the surface and in contrast $YO^-$ is homogeneously distributed inside the grain, in agreement with the Y enrichment of the Mg matrix (Table 2).

The ToF-SIMS analysis revealed a homogeneous enrichment in yttrium (probably as $Y_2O_3$ or $Y(OH)_3$)) and local enrichments in zirconium and to a less extent in neodymium of the oxides/hydroxides layer, corroborating previous studies [20,27,28].
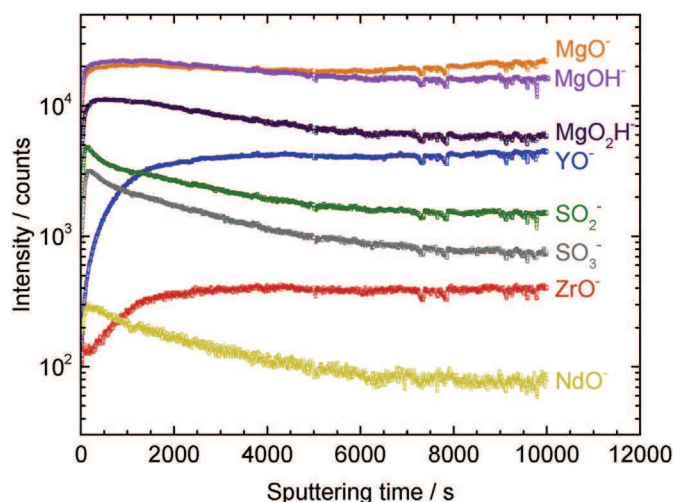
## 4. Discussion

The electrochemical behaviour of the WE43 Mg alloy was relatively similar in the NaCl and Na₂SO₄ solutions but there was, on the other hand, an influence of the electrolyte on the behaviour of the pure Mg (Figs. 3–5). From the impedance data analysis, it was possible to extract the oxides films thickness (Fig. 8b). Even if the values cannot be accurately determined, the complex-capacitance plots allowed the films thickness to be compared. It was shown that the films in the NaCl and Na₂SO₄ solutions were thinner for the WE43 alloy than for the pure Mg. Interestingly, although the polarisation curves and the impedance diagrams for the WE43 alloy appeared relatively comparable in both electrolytes (Figs. 3–5), the oxides film was thinner in the NaCl solution (Fig. 8). This is consistent with the breakdown of the oxides film (abrupt increase of the anodic current density) which was clearly seen in the chloride-containing solution (Fig. 3b). The aggressiveness of Cl⁻ was related for a part to their tendency to lose their hydration shell during the penetration in the film [51,52]. In addition, after about 24 h of immersion, the oxides films thickness remained constant over a period of at least 100 h (Fig. 8). This result can be explained by the fact that the films extended only laterally over the electrode



**Fig. 9.** ToF-SIMS depth profiles (negative ions) of the oxides/hydroxides film formed on the WE43 Mg alloy surface after 144 h of immersion in 0.1 M Na₂SO₄.
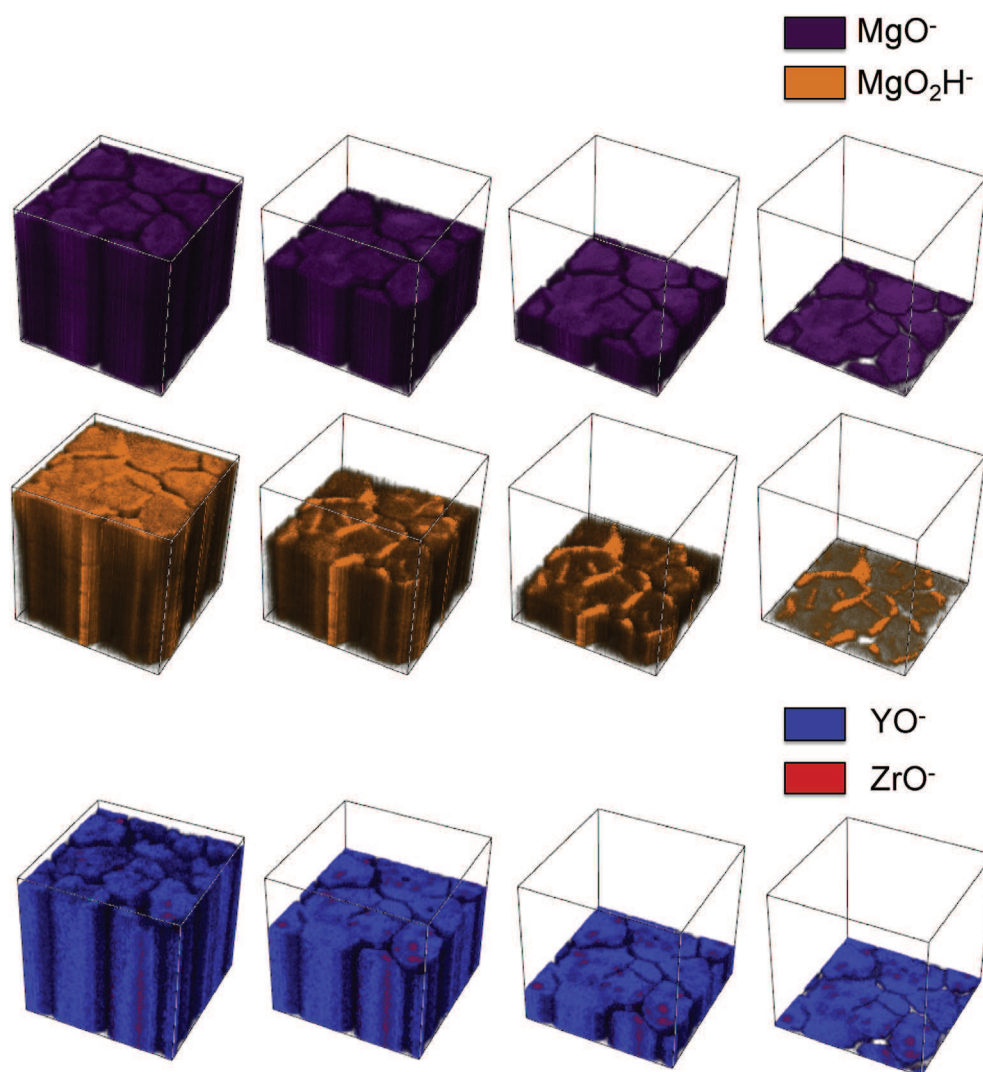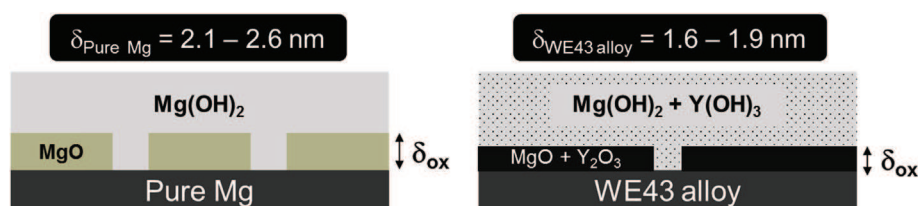


**Fig. 10.** 3D chemical imaging by ToF-SIMS analysis (negative mode) of the oxides/hydroxides film formed on the WE43 alloy surface. Only a few chosen ions are presented. The four images were acquired after 500 s, 4500 s, 9000 s and 12000 s of sputtering. Analysed surface area: 300 μm × 300 μm.

**Fig. 11.** Schematic illustration of the cross-section view of the oxides/hydroxides films formed on the pure Mg and on the WE43 Mg alloy surfaces after immersion in the $Na_2SO_4$ solution.

surfaces (progressive coverage with increasing immersion time). The oxides films growth was similar for both materials, mainly linked to the corrosion of the Mg matrix.

For the WE43 alloy, ToF-SIMS analysis showed an enrichment of the oxides/hydroxides layer by the alloying elements, such as yttrium (likely $Y_2O_3$ or $Y(OH)_3$) [26–28]. The smaller thickness of the oxides film for the Mg alloy can be explained by taking into account the Pilling-Bedworth (PB) ratio. For pure MgO, the PB ratio is inferior to 1 (0.8 [1,2,57]) indicating that the oxides film cannot completely covers the metal surface. In the case of Y, the PB ratio is greater than 1 (1.13 [57] or 1.39 [58]). The Mg oxide, enriched in Y, would be thinner and would have a higher coverage ability of the WE43 alloy surface. A schematic description of the oxides/hydroxides layer is shown in Fig. 11. The impedance diagrams obtained at the corrosion potential partly reflected the surface coverage by the oxides film, independently of the thickness. That is why the diagrams for the WE43 alloy were similar in the two electrolytes and the impedance values were almost twice those obtained for the pure Mg in the $Na_2SO_4$ solution (lower coverage). In the NaCl solution, due to the aggressiveness of $Cl^-$, the oxides/hydroxides layer formed on the pure Mg surface provided a limited protection. The impedance values were low (Figs. 4 and 5) and the electrode surface was strongly corroded (Fig. 6).

Finally, it can be mentioned that hydrogen gas is formed during the corrosion process and may penetrate into the Mg. This point was not discussed in the present work but it should be taken into account to have a more complete insight of the effect of the alloying elements on the corrosion behaviour of Mg alloys. It was recently shown that additions of <1 wt % of Zr or Nd to Mg greatly enhanced the hydrogen ingress [59].

## 5. Conclusions

The electrochemical behaviour of the WE43 Mg alloy was investigated in NaCl and $Na_2SO_4$ solutions and compared to that of pure Mg. From the analysis of the high-frequency part of the impedance diagrams, using the complex-capacitance plot, the films thickness was determined without the need of a fitting procedure. It revealed that the oxides film was about 35% thinner for the WE43 alloy than for the pure Mg in the $Na_2SO_4$ solution. ToF-SIMS analysis showed an enrichment of the corrosion products layer in Y and to a less extent in Zr and Nd. The incorporation of the alloying elements would be at the origin of the thinner and more stable oxides film in agreement with the increase of the Pilling-Bedworth ratio in the case of the WE43 alloy.

## Acknowledgements

## Appendix A. Supplementary data

Supplementary data to this article can be found online at https://doi.org/10.1016/j.electacta.2018.08.093.

## References

[1] M. Esmaily, J.E. Svensson, S. Fajardo, N. Birbilis, G.S. Frankel, S. Virtanen, R. Arrabal, S. Thomas, L.G. Johansson, Fundamentals and advances in magnesium alloy corrosion, Prog. Mater. Sci. 89 (2017) 92–193.

[2] F. Cao, G.L. Song, A. Atrens, Corrosion and passivation of magnesium alloys, Corros. Sci. 111 (2016) 835–845.

[3] M. Bannister, A. Mouritz, Magnesium alloys for aerospace structures, in: Introd. To Aerosp. Mater., 2009, pp. 224–231.

[4] A.P. Mouritz, Introduction to Aerospace Materials, Woodhead Publishing, 2012.

[5] C. Liu, S. Lu, Y. Fu, H. Zhang, Flammability and the oxidation kinetics of the magnesium alloys AZ31, WE43, and ZE10, Corros. Sci. 100 (2015) 177–185.

[6] F. Czerwinski, Controlling the ignition and flammability of magnesium for aerospace applications, Corros. Sci. 86 (2014) 1–16.

[7] J.H. Nordlien, K. Nisancioglu, S. Ono, N. Masuko, Morphology and structure of oxide films formed on MgAl alloys by exposure to air and water, J. Electrochem. Soc. 143 (1996) 2564–2572.

[8] J.H. Nordlien, K. Nisancioglu, S. Ono, N. Masuko, Morphology and structure of water-formed oxides on ternary MgAl alloys, J. Electrochem. Soc. 144 (1997) 461–466.

[9] G. Baril, C. Blanc, N. Pébère, AC impedance spectroscopy in characterizing time-dependent corrosion of AZ91 and AM50 magnesium alloys − characterization with respect to their microstructures, J. Electrochem. Soc. 148 (2001) B489–B496.

[10] M. Esmaily, D.B. Blücher, J.E. Svensson, M. Halvarsson, L.G. Johansson, New insights into the corrosion of magnesium alloys − the role of aluminum, Scripta Mater. 115 (2016) 91–95.

[11] A.D. Südholz, K. Gusieva, X.B. Chen, B.C. Muddle, M.A. Gibson, N. Birbilis, Electrochemical behaviour and corrosion of Mg-Y alloys, Corros. Sci. 53 (2011) 2277–2282.

[12] N. Birbilis, M.A. Easton, A.D. Sudholz, S.M. Zhu, M.A. Gibson, On the corrosion of binary magnesium-rare earth alloys, Corros. Sci. 51 (2009) 683–689.

[13] K. Gusieva, C.H.J. Davies, J.R. Scully, N. Birbilis, Corrosion of magnesium alloys: the role of alloying, Int. Mater. Rev. 60 (2015) 169–194.

[14] T. Cain, L.G. Bland, N. Birbilis, J.R. Scully, A compilation of corrosion potentials for magnesium alloys, Corrosion 70 (2014) 1043–1051.

[15] A.D. Südholz, N.T. Kirkland, R.G. Buchheit, N. Birbilis, Electrochemical properties of intermetallic phases and common impurity elements in magnesium alloys, Electrochem. Solid State Lett. 14 (2011) C5–C7.

[16] D.S. Gandel, M.A. Easton, M.A. Gibson, T. Abbott, N. Birbilis, The influence of zirconium additions on the corrosion of magnesium, Corros. Sci. 81 (2014) 27–35.

[17] W. Liu, F. Cao, Y. Xia, L. Chang, J. Zhang, Localized corrosion of magnesium alloys in NaCl Solutions explored by scanning electrochemical microscopy in feedback mode, Electrochim. Acta 132 (2014) 377–388.

[18] J. Liu, Y. Song, J. Chen, P. Chen, D. Shan, E.-H. Han, The special role of anodic second phases in the micro-galvanic corrosion of EW75 Mg alloy, Electrochim. Acta 189 (2016) 190–195.

[19] Y.L. Song, Y.H. Liu, S.R. Yu, X.Y. Zhu, S.H. Wang, Effect of neodymium on microstructure and corrosion resistance of AZ91 magnesium alloy, J. Mater. Sci. 42 (2007) 4435–4440.

[20] R. Pinto, M.G.S. Ferreira, M.J. Carmezim, M.F. Montemor, The corrosion behaviour of rare-earth containing magnesium alloys in borate buffer solution, Electrochim. Acta 56 (2011) 1535–1545.

[21] T. Takenaka, T. Ono, Y. Narazaki, Y. Naka, M. Kawakami, Improvement of corrosion resistance of magnesium metal by rare earth elements, Electrochim. Acta 53 (2007) 117–121.

[22] R. Pinto, M.G.S. Ferreira, M.J. Carmezim, M.F. Montemor, Passive behavior of magnesium alloys (Mg-Zr) containing rare-earth elements in alkaline media, Electrochim. Acta 55 (2010) 2482–2489.

[23] H. Wang, Y. Li, F. Wang, Influence of cerium on passivity behavior of wrought AZ91 alloy, Electrochim. Acta 54 (2008) 706–713.

[24] A.D. Südholz, N. Birbilis, C.J. Bettles, M.A. Gibson, Corrosion behaviour of Mg-alloy AZ91E with atypical alloying additions, J. Alloys Compd. 471 (2009) 109−115.

[25] T.J. Luo, Y.S. Yang, Y.J. Li, X.G. Dong, Influence of rare earth Y on the corrosion behavior of as-cast AZ91 alloy, Electrochim. Acta 54 (2009) 6433−6437.

[26] M. Liu, P. Schmutz, P.J. Uggowitzer, G. Song, A. Atrens, The influence of yttrium (Y) on the corrosion of Mg-Y binary alloys, Corros. Sci. 52 (2010) 3687−3701.

[27] F. Zucchi, V. Grassi, A. Frignani, C. Monticelli, G. Trabanelli, Electrochemical behaviour of a magnesium alloy containing rare earth elements, J. Appl. Electrochem. 36 (2006) 195−204.

[28] H. Ardelean, A. Seyeux, S. Zanna, F. Prima, I. Frateur, P. Marcus, Corrosion processes of Mg-Y-Nd-Zr alloy in $Na_2SO_4$ electrolyte, Corros. Sci. 73 (2013) 196−207.

[29] W. Xu, N. Birbilis, G. Sha, Y. Wang, J.E. Daniels, Y. Xiao, M. Ferry, A high-specific-strenght and corrosion-resistant magnesium alloy, Nat. Mater. 14 (2015) 1229−1236.

[30] M. Benoit, C. Bataillon, B. Gwinner, F. Miserque, M.E. Orazem, C.M. Sánchez-sánchez, B. Tribollet, V. Vivier, Comparison of different methods for measuring the passive film thickness on metals, Electrochim. Acta 201 (2016) 340−347.

[31] T. Barrès, B. Tribollet, O. Stephan, H. Montigaud, M. Boinet, Y. Cohin, Characterization of the porosity of silicon nitride thin layers by electrochemical impedance spectroscopy, Electrochim. Acta 227 (2017) 1−6.

[32] S. Chakri, I. Frateur, M.E. Orazem, E.M.M. Sutter, T.T.M. Tran, B. Tribollet, V. Vivier, Improved EIS analysis of the electrochemical behaviour of carbon steel in alkaline solution, Electrochim. Acta 246 (2017) 924−930.

[33] Y. Ben Amor, E. Sutter, H. Takenouti, B. Tribollet, M. Boinet, R. Faure, J. Balencie, G. Durieu, Electrochemical study of the tarnish layer of silver deposited on glass, Electrochim. Acta 131 (2014) 89−95.

[34] B.A. Boukamp, A linear Kronig-Kramers transform test for immittance data validation, J. Electrochem. Soc. 142 (1995) 1885.

[35] G. Ben-Hamu, D. Eliezer, K.S. Shin, S. Cohen, The relation between microstructure and corrosion behavior of Mg-Y-RE-Zr alloys, J. Alloys Compd. 431 (2007) 269−276.

[36] P.-W. Chu, E.A. Marquis, Linking the microstructure of a heat-treated WE43 Mg alloy with its corrosion behavior, Corros. Sci. 101 (2015) 94−104.

[37] T. Rzychoń, A. Kiełbus, Microstructure of WE43 casting magnesium alloy, J. Achiev. Mater. Manuf. Eng. 21 (2007) 31−34.

[38] A.E. Coy, F. Viejo, P. Skeldon, G.E. Thompson, Susceptibility of rare-earth-magnesium alloys to micro-galvanic corrosion, Corros. Sci. 52 (2010) 3896−3906.

[39] T. Rzychoń, J. Michalska, A. Kiełbus, Corrosion resistance of Mg-RE-Zr alloys, Manuf. Eng. 21 (2007) 51−54.

[40] N. Pébère, C. Riéra, F. Dabosi, Investigation of magnesium corrosion in aerated sodium sulfate solution by electrochemical impedance spectroscopy, Electrochim. Acta 35 (1990) 555−561.

[41] G. Baril, N. Pébère, The corrosion of pure magnesium in aerated and deaerated sodium sulphate solutions, Corros. Sci. 43 (2001) 471−484.

[42] M. Ascencio, M. Pekguleryuz, S. Omanovic, An investigation of the corrosion mechanisms of WE43 Mg alloy in a modified simulated body fluid solution: the influence of immersion time, Corros. Sci. 87 (2014) 489−503.

[43] M. Ascencio, M. Pekguleryuz, S. Omanovic, An investigation of the corrosion mechanisms of WE43 Mg alloy in a modified simulated body fluid solution: the effect of electrolyte renewal, Corros. Sci. 87 (2015) 297−310.

[44] G. Baril, G. Galicia, C. Deslouis, N. Pébère, B. Tribollet, V. Vivier, An impedance investigation of the mechanism of pure magnesium corrosion in sodium sulfate solutions, J. Electrochem. Soc. 154 (2007) C108−C113.

[45] S. Feliu Jr., I. Llorente, Corrosion product layers on magnesium alloys AZ31 and AZ61: surface chemistry and protective ability, Appl. Surf. Sci. 347 (2015) 736−C746.

[46] T.W. Cain, I. Gonzalez-Afanador, N. Birbilis, J.R. Scully, The role of surface films and dissolution products on the negative difference effect for magnesium: comparison of Cl⁻ versus Cl⁻ free solutions, J. Electrochem. Soc. 164 (2017) C300−C311.

[47] M. Taheri, M. Danaie, J.R. Kish, TEM examination of the film formed on corroding Mg prior to breakdown, J. Electrochem. Soc. 161 (2014) C89−C94.

[48] M.P. Brady, G. Rother, L.M. Anovitz, K.C. Littrell, K.A. Unocic, H.H. Elsentriecy, G.-L. Song, J.K. Thomson, N.C. Gallego, B. Davis, Film breakdown and nano-porous $Mg(OH)_2$ formation from corrosion of magnesium alloys in salt solutions, J. Electrochem. Soc. 162 (2015) C140−C149.

[49] G.-L. Song, K.A. Unocic, The anodic surface film and hydrogen evolution on Mg, Corros. Sci. 98 (2015) 758−765.

[50] N. Hara, Y. Kobayashi, D. Kagaya, N. Akao, Formation and breakdown of surface films on magnesium and its alloys in aqueous solutions, Corros. Sci. 49 (2007) 166−175.

[51] J.L. Trompette, L. Arurault, S. Fontorbes, L. Massot, Influence of the anion specificity on the electrochemical corrosion of anodized aluminum substrates, Electrochim. Acta 55 (2010) 2901−2910.

[52] J.L. Trompette, L. Massot, L. Arurault, S. Fontorbes, Influence of the anion specificity on the anodic polarization of titanium, Corros. Sci. 53 (2011) 1262−1268.

[53] A.D. King, N. Birbilis, J.R. Scully, Accurate electrochemical measurement of magnesium corrosion rates; a combined impedance, mass-loss and hydrogen collection study, Electrochim. Acta 121 (2014) 394−406.

[54] M. Stern, A.L. Geary, Electrochemical polarization, J. Electrochem. Soc. 104 (1957) 56.

[55] A.S. Nguyen, N. Causse, M. Musiani, M.E. Orazem, N. Pébère, B. Tribollet, V. Vivier, Determination of water uptake in organic coatings deposited on 2024 aluminium alloy: comparison between impedance measurements and gravimetry, Prog. Org. Coating 112 (2017) 93−100.

[56] W.M. Haynes, CRC Handbook of Chemistry and Physics, 97th Edition, 2017.

[57] S.D. Cramer, B.S. Covino Jr., Corrosion: Fundamentals, Testing, and Protection 13A, ASM Handbook, 2003.

[58] A.R. Mirak, C.J. Davidson, J.A. Taylor, Study on the early surface films formed on Mg-Y molten alloy in different atmospheres, J. Magn. Alloy 3 (2015) 173−179.

[59] M.P. Brady, A.V. Ievlev, M. Fayek, D.N. Leonard, M.G. Frith, H.M. Meyer III, A.J. Ramirez-Cuesta, L.L. Daemen, Y. Cheng, W. Guo, J.D. Poplawsky, O.S. Ovchinnikova, J. Thomson, L.M. Anovitz, G. Rother, D. Shin, G.-L. Song, B. Davis, Rapid diffusion and nanosegregation of hydrogen in magnesium alloys from exposure to water, ACS Appl. Mater. Interfaces 9 (2017) 38125−38134.